

Microscope objective for imaging atomic strontium with 0.63 micrometer resolution

I.H.A. KNOTTNERUS,^{1,*} S. PYATCHENKOV,¹ O.ONISHCHENKO,²
A.URECH,¹ G.A. SIVILOGLOU,^{1,3,*} AND F. SCHRECK¹

¹ *Van der Waals-Zeeman Institute, Institute of Physics, Faculty of Science, University of Amsterdam, Science Park 904, 1098 XH Amsterdam, The Netherlands*

² *LaserLaB, Department of Physics and Astronomy, VU University, De Boelelaan 1081, 1081 HV Amsterdam, The Netherlands*

³ *Shenzhen Institute for Quantum Science and Engineering, and Department of Physics, Southern University of Science and Technology, Shenzhen, 518055, People's Republic of China*

**microscope461@strontiumBEC.com*

Abstract: Imaging and manipulating individual atoms with submicrometer separation can be instrumental for quantum simulation of condensed matter Hamiltonians and quantum computation with neutral atoms. Quantum gas microscope experiments in most cases rely on quite costly solutions. Here we present an open-source design of a microscope objective for atomic strontium consisting solely of off-the-shelf lenses that is diffraction-limited for 461 nm light. A prototype built with a simple stacking design is measured to have a resolution of 0.63(4) μm , which is in agreement with the predicted value. This performance, together with the near diffraction-limited performance for 532 nm light makes this design useful for both quantum gas microscopes and optical tweezer experiments with strontium. Our microscope can easily be adapted to experiments with other atomic species such as erbium, ytterbium, and dysprosium, as well as Rydberg experiments with rubidium.

© 2022 Optical Society of America

1. Introduction

In the past decade, arrays of ultracold atoms have been proven an ideal system for quantum simulation [1] and a promising platform for quantum computation [2, 3]. Imaging and addressing single atoms is essential for progress in this direction and microscopy techniques have been developed for the case of ultracold quantum particles. More specifically, a top-down approach used by quantum gas microscopes (QGM) [4–6] is the loading of already quantum degenerate gases in site-resolved optical lattices while a bottom-up approach is based on individually filled and controlled optical tweezers [7–11]. The core necessity for both approaches is the availability of a high resolution objective that can resolve individual atoms at the single trap level.

The requirements on the performance of such an objective are highly demanding, including a long working distance, being corrected for the typically thick viewport of the vacuum chamber, and high resolution for a set of desired wavelengths, which can range from infrared to ultraviolet. Objectives fulfilling these requirements are in most cases not found off-the-shelf. Fortunately, in the study of quantum gases, only a single or a few wavelengths are of interest for atom imaging and manipulation. This is a huge simplification compared to the design of an achromatic objective and makes building an objective in house a cost-efficient possibility. Our objective is designed for detecting strontium on the $^1S_0 \leftrightarrow ^1P_1$ transition at a wavelength $\lambda = 461$ nm and should be suitable without modification for other atomic species with nearby transitions, such as ytterbium (399 nm), erbium (401 nm), and dysprosium (421 nm). Recent openly available designs attempted to exploit this characteristic of atomic systems, but their focus was on wavelengths longer than 550 nm [12, 13] that cannot serve the purpose of imaging atomic strontium.

The alkaline-earth element strontium [14] has two-valence electrons and properties that make it suitable for ultra-precise atomic clocks and quantum simulation [15, 16]. As was exploited

in very recent experiments with ultracold strontium in optical tweezers [17–20], and will be demonstrated in the next sections, the 461 nm transition can lead to submicrometer resolution for a numerical aperture that is not particularly high. To avoid over-complicating our apparatus our objective has to be placed outside the ultra-high vacuum chamber and thus has to be corrected for the 3.125 mm thick Corning HPFS fused silica viewport. This sets a stringent limitation to proximity of the optics to the atoms and thus a sufficiently large working distance (> 15 mm) is required. Single-site imaging for the great majority of ultracold atom experiments means a resolution that can enable imaging of atoms held by the optical lattice potential created by two counter propagating (usually 1064 nm) beams. Image processing can be used to enhance the resolving power of our microscope to obtain single-site detection [6]. To be able to simulate physics on the lattice, the objective needs to have a large field of view to resolve many lattice sites and preferably to have a resolution high enough for the manipulation and spin preparation of individual atoms using other relevant wavelengths. For strontium atoms, especially the long-lived $^1S_0 \leftrightarrow ^3P_0$ transition with $\lambda = 698$ nm and the $^1S_0 \leftrightarrow ^3P_2$ transition with $\lambda = 671$ nm are interesting for the purpose of state preparation and manipulation [21, 22]. Techniques involving, for example, magnetic field gradients or AC Stark shifts, can permit that even resolutions of around 1 μm are sufficient to already give single-site addressing of atoms [23]. It is also desirable that the depth of field is small enough that adjacent layers end up out of focus and do not distort the measurements.

Here, we report on a high-resolution, in-house manufactured, multilens microscope objective that can be used to image atomic strontium with the design procedure and the precise specifications openly-accessible. Our objective consists of a plastic tube that contains the lenses separated by spacers. The objective is tested by imaging an illuminated test target containing 200 nm diameter pinholes. The resolution of the objective is measured to be 0.63 μm for the primary wavelength of interest (461 nm) and always lower than 1.1 μm for different relevant colors of the illuminating light. The prototype has a diffraction-limited resolution for wavelengths 460 nm to 530 nm. Also, the field of view and depth of field of the objective are explored.

2. Design of the objective

2.1. Optical design

Our design takes [12] as a starting point and pushes the resolution by a factor of 2 compared to that work. The increased resolution is mandatory to reach our goals, even despite the advantage of using a smaller wavelength (461 nm instead of 780 nm), making the same NA result in a higher resolution. Simple readjustments of the lens distances were proven insufficient to reach the desired resolution. Our solution is to introduce an extra optical element for aberration correction.

The optical design of our objective is performed with the software OSLO. We now summarize the guiding principles of our approach. While minimizing on the RMS spot size and wavefront deviations, the distances between the lenses are varied in two steps: First, every position is taken as a free parameter in the fitting process in order to obtain an estimate for good values, which are then used as starting values for the next optimization steps. Then, the distance between any two lenses is varied individually, while compensating by refocusing the objective (i.e. varying the distance between the first lens and the viewport). The resulting configuration is presented in Table 1 and a cross section of the objective is shown in Fig 1. This design is predicted to be diffraction-limited for $\lambda = 461$ nm and to have a numerical aperture $\text{NA} = 0.44$. Using the Rayleigh criterion we obtain a resolution of 639 nm [24].

In addition to the main feature, which is the submicrometer resolution, the depth of field (DOF), the field of view (FOV) and tolerances on the placement of the individual lenses are explored since they are of importance when several layers of atoms separated by less than a micron have to be imaged. The DOF is modeled by translating the objective with respect to the viewport while keeping the target plane fixed and measuring the resolution of the microscope. The objective

#	Lens Type	Lens name	Manufacturer	\varnothing (mm)	Distance (mm)
1	Pos. Meniscus	LAM-459 ^a	Melles Griot	18.0	6.301
2	Pos. Meniscus	LE1076	Thorlabs	50.8	16.094
3	Pos. Meniscus	LE1418	Thorlabs	50.8	33.259
4	Biconvex	KBX-151	Newport	50.8	44.284
5	Plano-concave	LC1315	Thorlabs	50.8	73.108

Table 1: The lenses used to create the objective. All of these lenses are commercial lenses with anti-reflection coating in the range of 350 nm to 700 nm. The last column is the shortest distance of each lens to the air-side facet of the viewport.

^aThe LAM-459 model is deprecated, but can still be manufactured affordably on demand.

remains diffraction-limited over a range of 3.1 μm . This makes expensive nanopositioners unnecessary for our purposes and also does not limit our single-layer resolving ability, since the out-of-focus layers of atoms can in principle be isolated or removed [23]. Similarly, the FOV is modeled by sweeping over the acceptable range of incidence angles of the incoming light, yielding a FOV of about 200 μm . For a QGM with a lattice constant of 532 nm this corresponds to roughly 380 sites. In comparison, recent state-of-the-art experiments with ultracold gases used about 100 sites [25].

To determine the tolerances on the individual lenses, the relevant parameter (distance, decentering, tilt etc.) for a single lens is adjusted in the model, while the rest of the lenses are kept in their initial configuration. The objective is finally refocused by adjusting the distance between the first lens and the viewport. The main figure of merit is the RMS spot size of the system. We note that the first lens is not included in the tolerance testing process as the blurring due to the displacement of that lens can be corrected by adjusting the objective as a whole.

The design is remarkably robust to axial displacements, as all the lenses can be individually displaced more than 150 μm before the RMS spot size exceeds the diffraction limit. More problematic for the performance is the tilt of lenses, especially lens #4. At tilts larger than 0.03°, aberrations are increased and the performance of the objective drops significantly. This could be compensated by adjusting the tilt of the last lens (#5) accordingly, raising this limit to the much more tolerable value 0.05°. Two tolerances that should not be neglected when using commercial lenses is the center thickness and the decenter of the lenses. All lenses have a thickness tolerance of 100 μm and a decenter tolerance of 3 arcmin [26–28]. The decenter is modeled as the radial displacement from the optical axis and the maximum allowed value of 3 arcmin is detrimental for the performance, resulting in a RMS spot size exceeding the diffraction limit for almost every lens. If each lens is rotated such that the decenter is pointed in the same direction, the relative decenter decreases and the impact on the performance becomes manageable. This realization guided us to use slits in the objective tube for the adjustment of the lenses after the assembly of the objective, see Sec. 2.2. The numerical checks of the tolerances on the individual lenses are used as requirements for the housing. Monte-Carlo simulations of the correction procedures described here are performed and show that the success rate of our construction could be several ten percent. That meant that a few trials in placing the lenses would be enough to achieve diffraction-limited imaging as was verified empirically after we experimentally characterized our objective.

2.2. Mechanical design

The optical design targets dictate the requirements on the mechanical construction of the objective. The axial placement of the lenses can be off without detrimental effects by several tens of

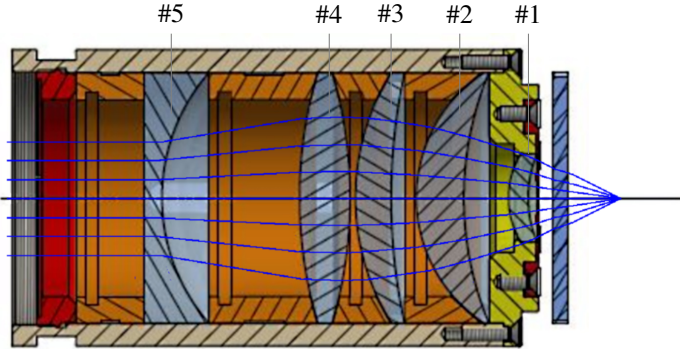


Fig. 1: The stacking design of the objective with modeled rays. Each lens is held in place with high precision spacing rings (orange). The assembly of lenses and spacing rings is fixed inside the tube with a locking ring (red). The first lens is mounted on a separate piece (yellow). The glass plate on the right depicts the viewport. All pieces are made out of PEEK.

micrometers and the lens tilt has to be preferably below 0.02° . The housing material of the objective has to be selected judiciously by taking into account the in-house manufacturing capabilities and requirements beyond lens placement, for example originating from the needs of atomic physics experiments. To prevent eddy currents from flowing when ramping the electromagnetic coils that surround the objective in our setup, the housing has to be made from a material with very low conductivity. At the same time, the stiffness and the low thermal expansion coefficient of the material are important for the robustness of the optical alignment.

For the housing of the objective a stacking model is chosen, following the example of [12, 29] but introducing several additional features, see Fig. 1. The lenses are placed inside an outer tube and are held in place by spacing rings that fit precisely between two adjacent lenses. The edges of the spacing rings are linear under angle to match the curvature of the lenses. The whole assembly is locked inside the outer tube by a threaded locking ring at the end. The first lens has a different diameter and is mounted on a separate piece that also serves as the cap of the outer tube. The additional features are the following: the outer tube is equipped with slits to guide and rotate the lenses for after-assembly adjustment, and six mirrors can be placed in the front piece to back-reflect laser light when aligning the objective to the vacuum chamber viewport. For pulling out the spacing rings, notches have been milled in each of the rings. CAD drawings of the design can be obtained on request.

This simple stacking model meets the requirements stated above. The spacing rings can be milled with several tens of micrometer precision. This matches directly the requirement on the axial placement and, given the 50.8 mm diameter of the rings, also matches the set requirement on the tilt of the lenses. The housing for our objective is made out of polyether ether ketone (PEEK), which is insulating and at the same time particularly convenient to machine. PEEK has a tensile modulus of 3.1 GPa to 3.8 GPa and a linear coefficient of thermal expansion of $4.7 \times 10^{-5} \text{ K}^{-1}$ to $5.5 \times 10^{-5} \text{ K}^{-1}$ [30].

3. Performance characterization

The resolution of the objective is obtained by directly measuring the point spread function (PSF) of the objective where the point source is in our case satisfactorily substituted by a back-illuminated glass plate coated with Cr and Pt-Pd containing 200 nm diameter holes provided by ETH Zürich. Using the Rayleigh criterion, the resolution for a point light source is defined as the distance

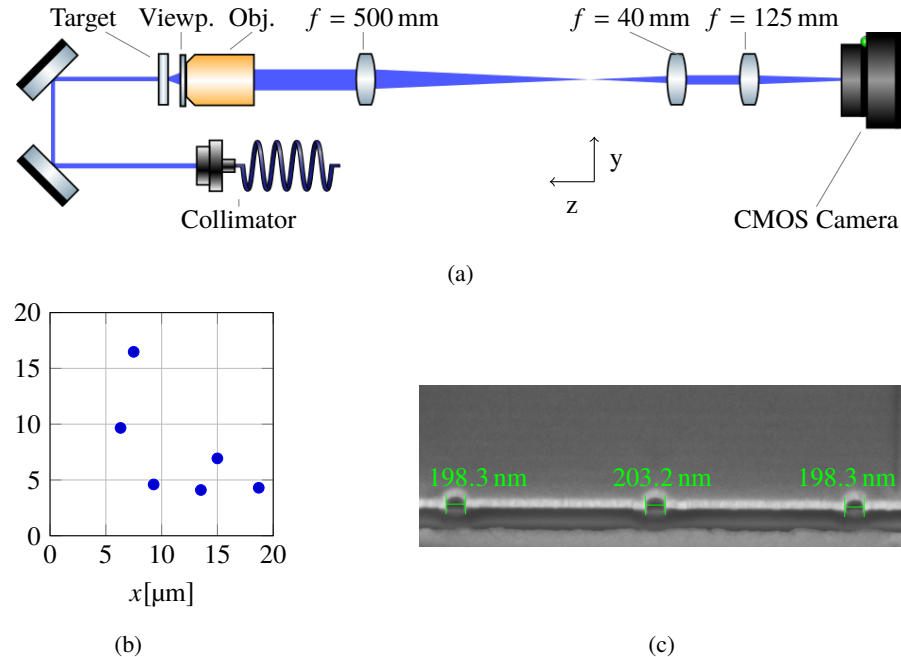


Fig. 2: Setup for characterizing the objective. (a) Overview of the setup. The target consists of a glass plate with a metal coating that has six 200 nm diameter holes. The target, objective and the 500 mm lens are mounted on translation stages. Drawing is not to scale. (b) Schematic drawing of the locations of the nanoholes on the test target. (c) SEM image of holes similar to those used in the target.

of the principle maximum of the PSF to the first minimum [24, 31]. For our objective with a predicted resolution of 639 nm the 200 nm diameter holes can be considered point sources. This assumption introduces an underestimation of the resolution by a couple nanometers, which is well below the measurement accuracy. A schematic of the setup used for testing the performance of the objective is shown in Fig. 2. The positioning of the holes is chosen to be non-periodic to avoid artifacts stemming from the Talbot effect [24, 32]. The objective images the diffraction pattern from the illuminated holes using a $f = 500$ mm achromatic doublet as field lens. To increase the magnification, $f = 40$ mm and $f = 125$ mm achromatic doublets are placed in a telescope configuration. The magnified pattern is imaged using a BlackFly CMOS camera with pixel size $5.6\mu\text{m}$. For ease of alignment, the upper row of elements in Fig. 2 is placed on an optical rail and the target (x, y-direction), objective (z-direction) and field lens (z-direction) are placed on translational stages.

In Fig. 3a, the observed pattern from the illuminated nanoholes is shown. The red cross-hairs denote the positions of the centers found using a Laplacian of Gaussian algorithm. We perform a calibration of the image by calculating the ratio between the distance in pixels and the SEM measured distance in μm for each pair of holes. In the case of Fig. 3a, this procedure gives an average calibration of $9.23(6)\text{ px}/\mu\text{m}$ over 15 distances. At each of the centers an azimuthal averaging has been performed to obtain a radial profile of the PSF of the objective for that spot, to which a Gaussian fit is made for the resolution, given by $I = I_0 \exp(-r^2/(2\sigma^2)) + a$, where I_0 is the peak intensity, σ is the standard deviation of the Gaussian and a is a constant for the read-out noise. The radial profile and fit for one nanohole is presented in Fig. 3b. The resolution of the objective is found as the average of the six fits and the error is defined by the standard

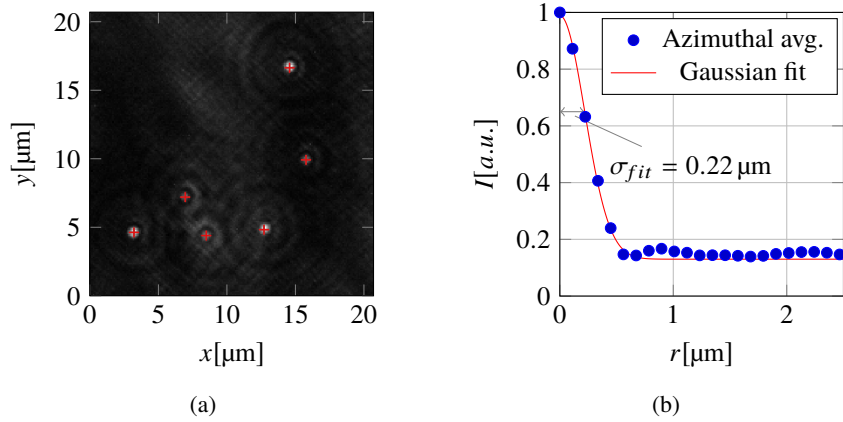


Fig. 3: Analysis of the objective's resolution. (a) Using a Laplacian of Gaussian algorithm each spot centre is detected and marked with red crosshairs. (b) An azimuthal average of the intensity of a single point. The red line shows a Gaussian fit through the data resulting in $\sigma_{fit} = 0.22 \mu\text{m}$, which corresponds to a resolution of $0.639 \mu\text{m}$ for 461 nm light.

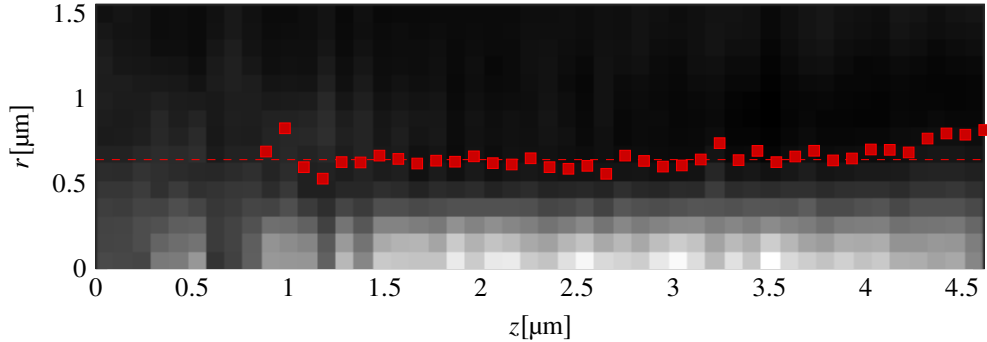


Fig. 4: Measurement of the through-focus PSF of the objective. The radial profile of the PSF is plotted for a range of z -values around the focus. The red dots denote the results for the fit of the resolution of the objective. The dashed line denotes the diffraction limit for 461 nm light of 639 nm. The objective is diffraction-limited from $1.1 \mu\text{m}$ to $4.2 \mu\text{m}$.

deviation in the sample, yielding $0.63(4) \mu\text{m}$.

The PSF as a function of position along the optical axis is measured by shifting the lens. Fig. 4 shows the normalized radial profile of the objective along this axis. Since for not properly focused spots, the Laplacian of Gaussian algorithm does not return satisfactory results, a single spot is cropped out and a 2D Gaussian fit is used to determine the center of the spot. For z -values far from the focus ($<0.8 \mu\text{m}$ in Fig. 4), the center of the spot contains too little intensity to be fitted properly and the resulting radial profiles are not a reliable measure. The red squares in Fig. 4 denote the values of the fitted resolution for the radial profile and the red dashed line lies at the diffraction limit of 639 nm. The dashed line denotes the diffraction limit at 639 nm. The objective is diffraction-limited from $1.1 \mu\text{m}$ to $4.2 \mu\text{m}$. This overlaps perfectly with the predicted DOF of $3.1 \mu\text{m}$.

The large field-of-view (FOV) is another important feature of our objective since it can permit the imaging and manipulation of thousands of particles. The FOV in our case is measured by

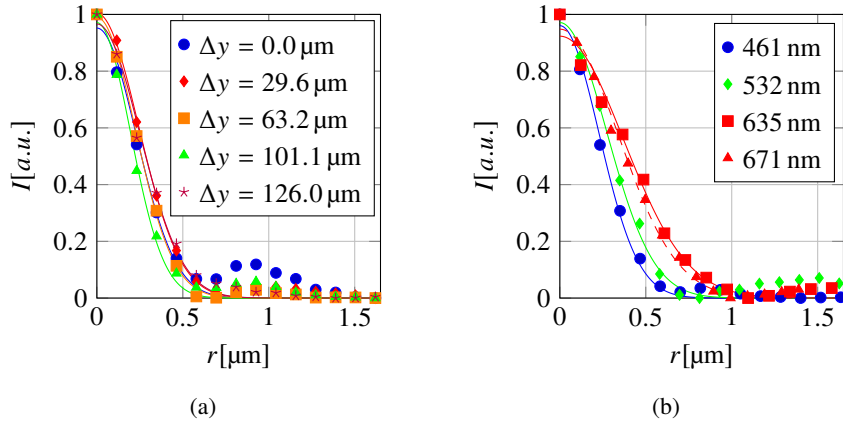


Fig. 5: Radial profiles of target hole images in dependence of (a) lateral displacement Δy of target hole from optical axis or (b) wavelength. Solid lines depict Gaussian fits to the data.

translating the target in front of the objective in the x, y -plane. Azimuthally integrated radial profiles for six positions during a translation of Δy along y are presented in Fig. 5a. To measure a large range, the CCD chip is positioned such that one edge was close to the position of best focus as judged by eye. The chip size then limits the measurement range to $\Delta y = 126 \mu\text{m}$. The resolution of the objective stays at the diffraction limit up to $100 \mu\text{m}$ displacement, which is smaller than the predicted FOV, but on the same order. The limited size of the CCD chip, together with the subjective placement of the chip by eye, might lead to an underestimation of the measured FOV.

When manipulating trapped strontium atoms for quantum simulation experiments, 671 nm or 698 nm light is often used because it addresses the ultranarrow transitions, which are important for e.g. clocks or the manipulation of nuclear spin states. Using the same setup, the objective is also tested for different wavelengths of illumination light. The resulting normalized radial profiles after refocusing are presented in Fig. 5b for 461 nm, 532 nm, 635 nm and 671 nm light. The measured resolutions are $0.63(4) \mu\text{m}$, $0.75(4) \mu\text{m}$, $1.09(9) \mu\text{m}$ and $1.05(4) \mu\text{m}$, respectively. The measured resolutions for both 461 nm and 532 nm are close to the diffraction limit within the error margin. The resolution is close to $1 \mu\text{m}$ for 671 nm light, which shows that this objective is also capable of single-site addressing of strontium.

4. Conclusion & Outlook

We have presented a design for a microscope objective consisting of commercially available lenses only that is diffraction-limited for 461 nm light. The objective is built using a simple stacking design and is measured to have a resolution of $0.63(4) \mu\text{m}$, which is in agreement with the predicted value. This performance, together with the near-diffraction limited performance for 532 nm light makes this design useful for both quantum gas microscopes and optical tweezer experiments with strontium. It also makes this design an interesting candidate for experiments with other atomic species such as erbium (401 nm), ytterbium (399 nm), and dysprosium (421 nm), as well as Rydberg experiments with rubidium (420 nm and 480 nm).

Acknowledgments

We thank Hans Ellermeijer from the Universiteit van Amsterdam Technology Center for his assistance in engineering the microscope objective. We also thank Joakim Reuteler of ScopeM, ETH Zürich for the manufacturing of the test target. This project has received funding from the

European Research Council (ERC) under the European Union's Seventh Framework Programme (FP7/2007-2013) (Grant agreement No. 615117 QuantStro). We thank the Netherlands Organisation for Scientific Research (NWO) for funding through Vici grant No. 680-47-619 and Gravitation grant No. 024.003.037, Quantum Software Consortium. G.S. thanks the European Commission for Marie Skłodowska-Curie grant SYMULGAS, No. 661171.

References

1. I. Bloch, J. Dalibard, and S. Nascimbène, "Quantum simulations with ultracold quantum gases," *Nat. Phys.* **8**, 267 (2012).
2. M. Saffman, "Quantum computing with neutral atoms," *Natl. Sci. Rev.* **6**, 24 (2018).
3. D. S. Weiss and M. Saffman, "Quantum computing with neutral atoms," *Phys. Today* **70**, 44 (2017).
4. S. Kuhr, "Quantum-gas microscopes: a new tool for cold-atom quantum simulators," *Natl. Sci. Rev.* **3**, 170 (2016).
5. W. S. Bakr, A. Peng, M. E. Tai, R. Ma, J. Simon, J. I. Gillen, S. Foelling, L. Pollet, and M. Greiner, "Probing the superfluid-to-Mott insulator transition at the single-atom level," *Science* **329**, 547 (2010).
6. J. F. Sherson, C. Weitenberg, M. Endres, M. Cheneau, I. Bloch, and S. Kuhr, "Single-atom-resolved fluorescence imaging of an atomic Mott insulator," *Nature* **467**, 68 (2010).
7. A. Ashkin, J. M. Dziedzic, J. E. Bjorkholm, and S. Chu, "Observation of a single-beam gradient force optical trap for dielectric particles," *Opt. Lett.* **11**, 288 (1986).
8. H. Bernien, S. Schwartz, A. Keesling, H. Levine, A. Omran, H. Pichler, S. Choi, A. S. Zibrov, M. Endres, M. Greiner, V. Vuletic, and M. D. Lukin, "Probing many-body dynamics on a 51-atom quantum simulator," *Nature* **551**, 579 (2017). Article.
9. D. Barredo, S. de Léséleuc, V. Lienhard, T. Lahaye, and A. Browaeys, "An atom-by-atom assembler of defect-free arbitrary two-dimensional atomic arrays," *Science* **354**, 1021 (2016).
10. N. Schlosser, G. Reymond, I. Protsenko, and P. Grangier, "Sub-Poissonian loading of single atoms in a microscopic dipole trap," *Nature* **411**, 1024 (2001).
11. D. Barredo, V. Lienhard, S. de Léséleuc, T. Lahaye, and A. Browaeys, "Synthetic three-dimensional atomic structures assembled atom by atom," *Nature* **561**, 79 (2018).
12. L. M. Bennie, P. T. Starkey, M. Jasperse, C. J. Billington, R. P. Anderson, and L. D. Turner, "A versatile high resolution objective for imaging quantum gases," *Opt. Express* **21**, 9011 (2013).
13. X. Li, F. Zhou, M. Ke, P. Xu, X.-D. He, J. Wang, and M.-S. Zhan, "High-resolution ex vacuo objective for cold atom experiments," *Appl. Opt.* **57**, 7584 (2018).
14. S. Stellmer, M. K. Tey, B. Huang, R. Grimm, and F. Schreck, "Bose-Einstein condensation of strontium," *Phys. Rev. Lett.* **103**, 200401 (2009).
15. S. L. Campbell, R. B. Hutson, G. E. Marti, A. Goban, N. Darkwah Oppong, R. L. McNally, L. Sonderhouse, J. M. Robinson, W. Zhang, B. J. Bloom, and J. Ye, "A Fermi-degenerate three-dimensional optical lattice clock," *Science* **358**, 90 (2017).
16. M. J. Martin, M. Bishof, M. D. Swallows, X. Zhang, C. Benko, J. von Stecher, A. V. Gorshkov, A. M. Rey, and J. Ye, "A quantum many-body spin system in an optical lattice clock," *Science* **341**, 632 (2013).
17. A. Cooper, J. P. Covey, I. S. Madjarov, S. G. Porsev, M. S. Safronova, and M. Endres, "Alkaline-earth atoms in optical tweezers," *Phys. Rev. X* **8**, 041055 (2018).
18. M. A. Norcia, A. W. Young, and A. M. Kaufman, "Microscopic control and detection of ultracold strontium in optical-tweezer arrays," *Phys. Rev. X* **8**, 041054 (2018).
19. J. P. Covey, I. S. Madjarov, A. Cooper, and M. Endres, "2000-times repeated imaging of strontium atoms in clock-magic tweezer arrays," *Phys. Rev. Lett.* **122**, 173201 (2019).
20. N. C. Jackson, R. K. Hanley, M. Hill, C. S. Adams, and M. P. A. Jones, "Number-resolved imaging of ^{88}Sr atoms in a long working distance optical tweezer," *arXiv:1904.03233* (2019).
21. A. D. Ludlow, M. M. Boyd, J. Ye, E. Peik, and P. O. Schmidt, "Optical atomic clocks," *Rev. Mod. Phys.* **87**, 637 (2015).
22. O. Onishchenko, S. Pyatchenkov, A. Urech, C.-C. Chen, S. Bennetts, G. A. Siviloglou, and F. Schreck, "Frequency of the ultranarrow $^1\text{S}_0 - ^3\text{P}_2$ transition in ^{87}Sr ," *Phys. Rev. A* **99**, 052503 (2019).
23. K. Shibata, R. Yamamoto, Y. Seki, and Y. Takahashi, "Optical spectral imaging of a single layer of a quantum gas with an ultranarrow optical transition," *Phys. Rev. A* **89**, 031601 (2014).
24. B. E. A. Saleh and M. C. Teich, *Fundamentals of Photonics* (Wiley, 2013).
25. A. Mazurenko, C. S. Chiu, G. Ji, M. F. Parsons, M. Kanász-Nagy, R. Schmidt, F. Grusdt, E. Demler, D. Greif, and M. Greiner, "A cold-atom Fermi-Hubbard antiferromagnet," *Nature* **545**, 462 (2017).
26. Thorlabs, "N-BK7 Positive Meniscus Lenses," https://www.thorlabs.com/newgroupage9.cfm?objectgroup_id=130.
27. Thorlabs, "N-BK7 Positive Meniscus Lenses," https://www.thorlabs.com/newgroupage9.cfm?objectgroup_id=6509.
28. Newport Corporation, "KBX-151," <https://www.newport.com/p/KBX151>.
29. W. Alt, "An objective lens for efficient fluorescence detection of single atoms," *Optik* **113**, 142 (2002).

30. K. Van de Velde and P. Kiekens, "Thermoplastic polymers: overview of several properties and their consequences in flax fibre reinforced composites," *Polym. Test.* **20**, 885 (2001).
31. F. Rayleigh, "Investigations in optics, with special reference to the spectroscope," *Phil. Mag.* **5**, **8**, 261 (1879).
32. H. F. Talbot, "Facts relating to optical science," *Phil. Mag.* **4**, **9**, 401 (1836).